

Experimental study of beam hardening artifacts in photon counting breast computed tomography

M.G. Bisogni^a, A. Del Guerra^a, N. Lanconelli^b, A. Lauria^c, G. Mettivier^c, M.C. Montesi^{c,*},
D. Panetta^a, R. Pani^d, M.G. Quattrocchi^a, P. Randaccio^e, V. Rosso^a, P. Russo^c

^a*Dip. di Fisica, Univ. di Pisa and INFN, Pisa, Italy*

^b*Dip. di Fisica, Univ. di Bologna and INFN, Bologna, Italy*

^c*Dip. di Scienze Fisiche, Univ. di Napoli Federico II and INFN, Napoli, Italy*

^d*Dip. di Medicina Sperimentale, Univ. La Sapienza and INFN, Roma, Italy*

^e*Dip. di Fisica, Univ. di Cagliari and INFN, Cagliari, Italy*

Available online 27 July 2007

Abstract

We are implementing an X-ray breast Computed Tomography (CT) system on the gantry of a dedicated single photon emission tomography system for breast Tc-99 imaging. For the breast CT system we investigated the relevance of the beam hardening artifact. We studied the use of a single photon counting silicon pixel detector (0.3 mm thick, 256 × 256 pixel, 55 μm pitch, bump-bonded to the Medipix2 photon counting readout chip) as detector unit in our X-ray CT system. We evaluated the beam hardening “cupping” artifact using homogeneous PMMA slabs and phantoms up to 14 cm in diameter, used as uncompressed breast tissue phantoms, imaged with a tungsten anode tube at 80 kVp with 4.2 mm Al filtration. For beam hardening evaluation we used a bimodal energy model. The CT data show a “cupping” artifact going from 4% (4-cm thick material) to 18% (14-cm thick material). This huge artifacts is influenced by the low detection efficiency and the charge sharing effect of the silicon pixel detector.

© 2007 Published by Elsevier B.V.

PACS: 85.57.cp; 87.57.Q

Keywords: Beam hardening artifacts; Single photon counting detector; Breast CT

1. Introduction

We are implementing an X-ray Computed Tomography (CT) system on the gantry of a dedicated, scintillator-based single photon emission tomography (SPECT) system for breast Tc-99m imaging, under realization in the framework of a national project for new imaging techniques for breast cancer diagnosis [1]. The integration of a compact CT head could allow for anatomical co-registration of the X-ray CT slices (with a design resolution of ≈ 1 mm) with the radionuclide tomographic slices recorded with the SPECT system (intended to detect, with $\text{SNR} > 5$, breast tumours of about 8 mm diameter). For the X-ray detector, we are

investigating the use of a semiconductor-based single photon counting detector bump-bonded to the Medipix2 readout chip developed by the Medipix2 European collaboration (www.cern.ch/medipix) [2]. In the combined SPECT/CT system, the breast would be scanned in a pendant geometry, i.e., with the patient in a prone position and the breast uncompressed. The requirements for this X-ray CT imaging task would imply a significant beam hardening artifact in the CT images due to density-drop at the centre of the large CT reconstructed slice. In fact, it is well known that the use of a polychromatic X-ray source in CT implies that the relationship between the logarithmic attenuation and the absorber thickness is not linear, as occurs for a monochromatic beam [3,4]. Since the logarithmic attenuation signal registered in CT projections is not linear with the sample thickness, the reconstructed

*Corresponding author.

E-mail address: montesi@na.infn.it (M.C. Montesi).

images show various artifacts. In particular, the beam energy distribution becomes more abundant in high-energy photons and this effect causes an under-estimation or cupping artifact [4] in the reconstructed attenuation coefficient at the centre of the sampled volume. The cupping effect can be quantified by the line profile of the reconstructed attenuation coefficient (or of CT numbers) along an axis through the object. It has been shown [5,6] that the extent of this artifact depends also on the detection process. In fact, different types of imaging detectors (energy integrating, energy weighting, or photon counting detectors) assign a different weight to each detected X-ray photon. In photon counting mode, as in the case of this study, the detector adds a count in the pixel counter for any photon releasing in the detector pixel an energy higher than a preset threshold, independent of the photon energy: then, the assigned weight is the same for all interacting photons. This behaviour is different from that of energy integrating detectors (e.g., flat panel detectors as used for digital radiography), where the contribution of each photon to the integrated signal is proportional to its deposited energy. This condition effectively discriminates the way in which low- and high-energy photons produce a signal in the detector, and this influences the relevance of the beam hardening effect in energy integrating detectors, with respect to photon counting detectors. Finally, energy weighting detectors are those which assign to each interacting photon of energy E , a weight other than constant or linearly increasing with E , optimized according to some criteria: for example, the weight can be proportional to $1/E^3$, if one wants to maximize the signal-to-noise ratio [5]. To our knowledge, this particular analysis of the relevance of the detection process in digital radiography has first been pointed out by the Medipix2 group at Erlangen University [5] and its application to the beam hardening effect in CT has been analysed in detail recently in a simulation study [6]. In particular, it has been shown [6] that in photon counting mode, the effect of beam hardening in X-ray CT could be reduced with respect to energy weighting detectors and worsened with respect to charge integrating detectors. The beam artifact can be reduced either in pre-reconstruction [4] or in post-reconstruction [7] by low-energy filtering of the input X-ray beam or by linearization of the detector output. In evaluating the beam hardening artifact in CT, we will follow the bimodal energy model as in Ref. [3], whereas for a given polychromatic beam the X-ray attenuation in a material is described by two effective energies (E_1 , E_2 ; $E_2 > E_1$) and, correspondingly, by two effective attenuation coefficients μ_1 and μ_2 ($\mu_2 < \mu_1$). The lower value μ_2 at the beam effective energy E_2 accounts for the effective attenuation in large material thicknesses. In order to evaluate the relevance of this phenomenon in our photon counting X-ray breast CT system, we measured the beam hardening cupping artifact in homogeneous PMMA phantoms that simulate the average uncompressed breast tissue.

2. Experimental set-up

2.1. Breast phantoms and dose measurements

We used homogeneous PMMA (Lucite, density = 1.19 g/cm^3) phantoms that simulate the breast tissue attenuation (Fig. 1(a)). A first phantom was a PMMA cylinder with 14 cm diameter and 15 cm height. This diameter corresponds to the average value ($14.04 \pm 2.16 \text{ cm}$) of the distribution of breast diameters at the chest wall, reported on a group of 200 women [8]. A second phantom is a PMMA block shaped in a form simulating a pendant breast (Fig. 1(b)) containing a half-ellipsoid of rotation with half-axis of 7, 7 and 10.5 cm, respectively. The beam hardening effect was also evaluated with measurements of logarithmic attenuation in a stack of 1 up to 14 PMMA sheets ($20 \times 20 \text{ cm}^2$, 1 cm thick). The use of material slabs instead of shaped samples in the same irradiation geometry allows to evaluate the beam hardening artifact independent of the sample geometry. Using PMMA sheets, we determined the parameters of the beam hardening model used in this study (Section 2.2). Entrance dose measurements have been performed with a 0.6 cm^3 pencil ionization chamber (PTW–Freiburg, Germany) positioned in air at the isocentre of the CT system.

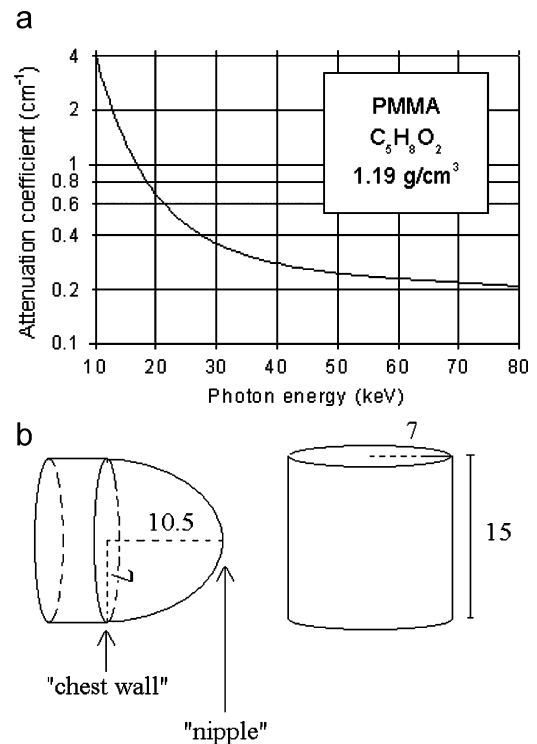


Fig. 1. (a) PMMA (lucite) attenuation coefficient versus energy, as deduced from the NIST database (<http://physics.nist.gov/PhysRefData>); (b) ellipsoidal-shaped PMMA block (derived from a 14-cm-diameter cylinder) and PMMA cylindrical phantom used as breast tissue phantoms (dimensions in cm).

2.2. X-ray sources and spectroscopy

Our breast CT system uses a continuous wave X-ray tube with W anode with a 40 μm focal spot size (Source-Ray, Inc., mod. SB-80-250, NY, USA). The tube voltage has been set from 35 to 80 kVp with an anode current of 250 μA . The tube has an inherent filtration equivalent to 1.8 mm Al; 2.4 mm Al was added, for a total of 4.2 mm Al equivalent filtration. The measured Half Value Layer of this X-ray beam was 7.2 mm Al. A tungsten collimator was used to obtain a fan beam irradiation geometry (4° horizontal \times 56° vertical). The detector used for measuring the X-ray spectrum incident on, or transmitted from the PMMA phantom, is a CdTe diode detector (mod. XR-100T-CdTe) with its associated power supply and amplifier (mod. PX2T-CR) from Amptek Inc., Bedford, MA, USA. Its Rise Time Discrimination option was not used. This CdTe detector is 1 mm thick and its detection efficiency is 100% up to 50 keV and 85% at 80 keV. A tungsten aperture (0.2 mm diameter) was used as a collimator in front of the CdTe detector in order to reduce the photon flux. The X-ray intensity $f(E)\gamma(E)$ (photons $\text{s}^{-1}\text{mm}^{-2} \text{mA}^{-1} \text{keV}^{-1}$) was measured at 80 kVp and at 51.5 cm focus-to-detector distance as a function of the photon energy E for the incident intensity $f_0(E)\gamma(E)$ and for the transmitted intensity $f_x(E)\gamma(E)$ after a thickness x of PMMA. The quantity $f(E)\gamma(E)$ (source–detector efficiency, [3]) is the product of the X-ray beam intensity $f(E)$ and the detector efficiency (E). Then, we calculated the integrated intensities $I_x = \int f_x(E)\gamma(E) dE$ and $I_0 = \int f_0(E)\gamma(E) dE$ and the logarithmic attenuation was derived as $-\ln(I_x/I_0)$. It has been shown [3] that the X-ray logarithmic attenuation can be well described by the three-parameters model given by:

$$-\ln(I_x/I_0) = \mu_2 x + \ln\{[1 + \alpha]/[1 + \alpha \exp(\mu_2 x - \mu_1 x)]\}. \quad (1)$$

As a special case of this formula, for large material thicknesses, the logarithmic attenuation follows a linear trend versus the material thickness x , given by

$$-\ln(I_x/I_0) = \mu_2 x + \ln(1 + \alpha) \quad (2)$$

where

$$\alpha = f(E_1)\gamma(E_1)/f(E_2)\gamma(E_2). \quad (3)$$

E_1 and E_2 being two effective energies describing the attenuation process in a material irradiated with a polychromatic X-ray beam. Hence, according to this bimodal energy model, the coefficient $\mu_2 = \mu(E = E_2)$ can be evaluated from measurements of logarithmic attenuation in increasing thickness material slabs as the slope of the linear fitting curve at large thicknesses, and the parameter α is the intercept of this linear fit in a plot of $(-\ln I_x/I_0)$ versus material thickness x . For small thicknesses (e.g., $x \ll 1$ cm), the model (1) reduces to

$$-\ln(I_x/I_0) = \mu_2 x + [\alpha/(1 + \alpha)(\mu_1 - \mu_2)]x. \quad (4)$$

2.3. CT set-up and software

Our prototype X-ray breast CT system (Fig. 2) is composed of a fixed X-ray tube, a single photon counting silicon detector being translated in the direction of the fan beam and a motorized sample holder which allows for translating and rotating the breast phantoms in the X-ray beam. The X-ray source-to-detector distance is 64.5 cm; the system magnification is about 1.9 for a sample located at the isocentre. The photon counting silicon pixel detector is bump-bonded to the Medipix2 readout circuit. The detector features a 256×256 square pixels of 55 μm pitch, for a sensitive area of $1.4 \times 1.4 \text{ cm}^2$, operating at room temperature at a detector bias voltage of +100 V. The detection threshold (above which a photon is detected) was set at 12 keV. For the present work we have used a silicon detector 0.3 mm thick (quantum efficiency 3% for $E = 50$ keV). The $256 \times 256 \times 13$ bit data of a single acquisition are read out serially by a dedicated electronic interface connected to a commercial digital I/O board. The planar projections are acquired by a custom software, Medisoft 4.1, developed at University & INFN Napoli, and are reconstructed off-line with a custom software developed at University & INFN Pisa, implementing the filtered backprojection fan-beam reconstruction algorithm. The small sensitive area of the detector was accounted for by scanning linearly the transmitted X-ray field for each projection angle. The phantom being homogeneous, for practical reasons we performed just one projection (at 80 kVp, 7.5 mAs/projection) and replicated it for 180 viewing angles. For the cylindrical phantom, the transaxial field of view was 0.74 cm, and in the case of the ellipsoidal phantom, we imaged three slices 0.76-cm thick at three axial positions from the chest to the nipple (Fig. 1).

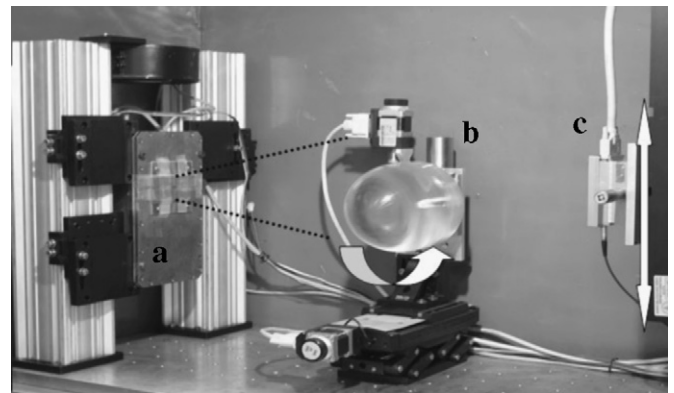


Fig. 2. CT experimental set-up: (a) W-anode X-ray tube with added Al filter and tungsten collimator (the dotted lines indicate a $4^\circ \times 56^\circ$ fan beam); (b) motorized translation and rotation stages for breast phantoms; (c) motorized translation stage for the photon counting Si detector (detector–isocentre distance 30.5 cm).

3. Results and discussion

3.1. Dose and spectroscopy measurements

The incident and transmitted X-ray spectra of the tungsten source (80 kVp) have been measured with the CdTe detector. The mean energy of the incident X-ray spectra was 47.3 keV and it increased to 51.2 keV after 14 cm of PMMA. The measured air kerma per unit mAs of our CT system (at 80 kVp, W-anode tube) at the isocentre (36 cm distance) was 470 Gy/mAs \pm 4%. This corresponds to a measured count rate of the photon counting silicon detector of 4.4×10^5 counts s⁻¹ mm⁻² mA⁻¹ at the isocentre.

3.2. Beam hardening in PMMA slabs

The incident intensity I_0 and the attenuated intensity I_x have been measured using the CdTe detector by stacking an increasing number (0, 1, 2, ..., 14) of 1-cm-thick PMMA sheets with the 80 kVp X-ray fan beam. In Fig. 3 the measured logarithmic attenuation is plotted against material thickness. The slope of the linear fit provides a value of the effective attenuation coefficient for large thicknesses of PMMA, $\mu_2 = 0.244 \pm 0.003$ cm⁻¹, corresponding to a beam effective (high) energy $E_2 = 51.0$ keV (Fig. 1). On the other hand, from the intercept of his linear fit we derived the value of the parameter $\alpha = 0.276$ (Eq. (1)). Then, from Eq. (3), with known μ_2 , and from the acquired spectra that provide $f(E)\gamma(E)$, we derived an estimate of the effective (low) energy $E_1 = 21.3$ keV and hence (Fig. 1), of the effective attenuation coefficient $\mu_1 = 0.602$ cm⁻¹. These values of the bimodal beam hardening model in Ref. [3] are valid for PMMA, with the given 80-kVp beam, for the given irradiation geometry and for the given CdTe detector efficiency. According to the model, and with the confidence in its valid application to our data resulting from the

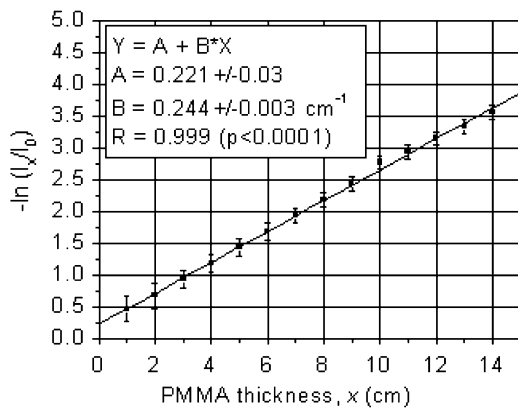


Fig. 3. (a) X-ray attenuation in PMMA as a function of material thickness. The spectral intensities have been integrated from 10 to 80 keV in order to give integrated intensities I_x and I_0 . The slope of the weighted least-squares linear fit (solid line) gives an effective attenuation coefficient of 0.244 cm⁻¹.

goodness of fit in Fig. 3, these three parameters (μ_1 , μ_2 , α) completely characterize the X-ray attenuation of PMMA.

3.3. Beam hardening in PMMA phantoms

The effect of beam hardening has been evaluated also on the CT reconstructed images of the two PMMA phantoms. The data were composed in large area projections for covering the whole phantom's projected area and were binned by 8×8 pixels, corresponding to an area of $440 \times 440 \mu\text{m}^2$. These projections were processed to form the fan-beam sinogram and then a filtered backprojection algorithm with ramp filter was applied. The CT reconstructions are shown in Fig. 4a (cylindrical phantom, single slice) and Fig. 5 (ellipsoid phantom). The 3D image, in which the voxel was a cube of 232 or 246 μm (for the 14 cm cylinder phantom, and for the ellipsoid-shaped phantom, respectively), was composed by stacking all the reconstructed slices (Fig. 5). The reconstructed attenuation profile of the PMMA cylinder ($\phi = 14$ cm), evaluated on a trans-axial slice, has been plotted in Fig. 4b. We evaluated a drop of the attenuation coefficient ($\mu_{\text{edge}} - \mu_{\text{centre}}$)/ μ_{edge} as large as 18% (from 0.33 to 0.27 cm⁻¹). In the case of the ellipsoid phantom, the reconstructed attenuation coefficient has been evaluated along a diameter

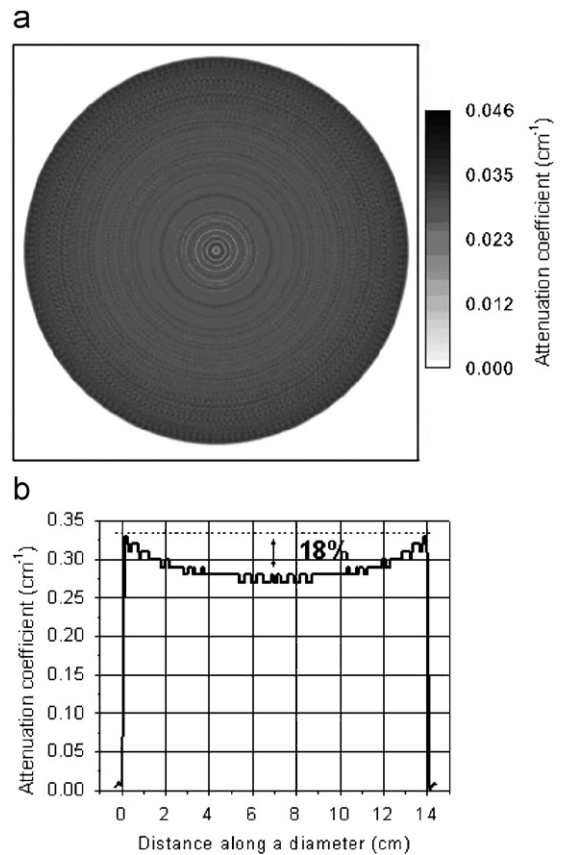


Fig. 4. (a) 2D reconstruction of a single slice (thickness = 232 μm) of the cylindrical phantom (isotropic voxel side = 232 μm , total slice thickness = 0.74 cm). A 2×2 pixel Gaussian blurring filter was applied; (b) attenuation profile along a diameter of the cylindrical phantom.

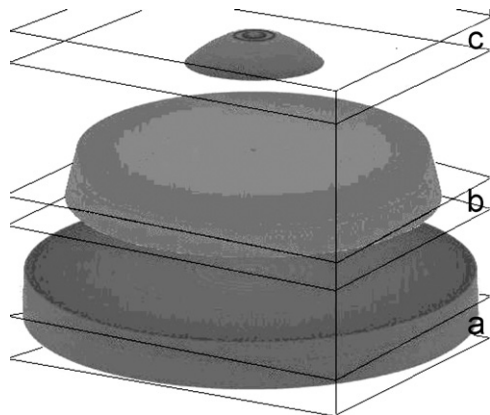


Fig. 5. 3D view of the CT reconstruction of three different sections of the PMMA ellipsoid phantom (isotropic voxel side = 246 μm) relative to three different distances from the phantom top nipple: (a) distance = 10.5 cm, slice thickness = 0.76 cm; (b) distance = 4.5 cm, slice thickness = 0.76 cm; (c) distance = 0.5 cm, slice thickness = 0.5 cm.

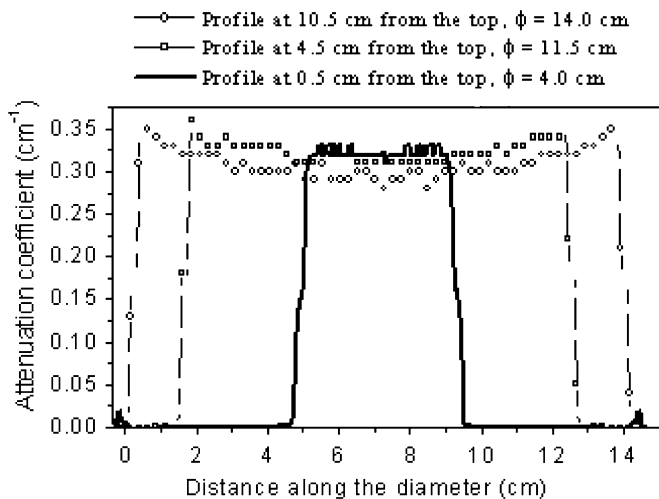


Fig. 6. Attenuation coefficient profiles of the three transaxial slices of the ellipsoid PMMA phantom relative to three different distances from the phantom top: 10.5, 4.5 and 0.5 cm, respectively. The slice thickness is 246 μm for each profile.

at three different distances along the longitudinal phantom axis, corresponding to three different depths from the phantom top nipple: 0.5, 4.5 cm (middle) and 10.5 cm (chest wall), respectively (Fig. 6). For the maximum diameter (= 14 cm) of the ellipsoid phantom, the attenuation coefficient drop is the same ($(\mu_{\text{edge}} - \mu_{\text{centre}}) / \mu_{\text{edge}} = 18\%$) as for the cylindrical phantom. For the middle diameter (= 11.5 cm), the beam hardening is about 12% and for the 4.5 cm diameter, the beam hardening artifact is about 4% (Fig. 6). In order to compare our measurements with the prediction of the bimodal energy model, we calculated the attenuation coefficient for a PMMA thickness of 14 cm. The beam hardening artifacts

calculated from Eq. (4) with the parameters determined in Section 3.2 is 19%. We point out that the values of the parameters of the bimodal energy model evaluated in Section 3.2 refer to the measurements made with a CdTe detector, while the CT measurements were made with a silicon pixel detector. Hence, the source–detector function $f(E)\gamma(E)$ is different in the two cases, due to the very different efficiency $\gamma(E)$ of the two detectors. In addition, the silicon pixel detector used in this study is known to exhibit a significant charge sharing effect [9] due its very fine pitch: this effect produces a distortion (increase) of the low-energy part of the X-ray spectrum. These two effects are expected to produce a shift towards lower energies of the source–detector efficiency and hence an increase of the beam hardening artifact of the Si with respect to the CdTe data. However, the extent of this large cupping artifact (18% from edge to centre of the 14 cm phantom) is in rough agreement with the prediction (19%) of the model with the parameters determined with the CdTe detector.

4. Conclusions

We reported on preliminary tests for the beam hardening cupping artifact in a photon counting X-ray breast CT system using PMMA phantoms and a very fine pitch silicon pixel detector. The CT data at 80 kVp show a decrease (from edge to center) of the attenuation coefficient of 4% when the PMMA thickness is 4 cm and of 18% for 14 cm PMMA thick material. A bimodal energy model for a beam hardening artifact in CT [3] was successfully applied to our data and produced an estimate of 19% for the central drop of the attenuation coefficient for the 14-cm-diameter phantom. In a future paper, a correction of the CT data in the pre-reconstruction phase will be applied and tests will be reported of this photon counting system in comparison with an energy integrating flat panel detector.

Acknowledgement

This work has been done in the framework of activities of MIUR-PRIN project 2004028450.

References

- [1] S. Vecchio, et al., A single photon emission computed tomography for breast cancer imaging, Presented at VCI 2007 Conference, Vienna 2007.
- [2] X. Llopart, et al., IEEE Trans. Nucl. Sci. NS-49 (2002) 2279.
- [3] E. Van de Castele, et al., Phys. Med. Biol. 47 (2002) 4181.
- [4] R.A. Brooks, G. Di Chiro, Phys. Med. Biol. 21 (1976) 390.
- [5] J. Geirsch, et al., Nucl. Instr. and Meth. A 531 (2004) 68.
- [6] P. Shikhaliev, Phys. Med. Biol. 50 (2005) 5813.
- [7] O. Nalcioğlu, R.Y. Lou, Phys. Med. Biol. 24 (1979) 330.
- [8] J.M. Boone, et al., Med. Phys. 31 (2004) 226.
- [9] B. Norlin, et al., Nucl. Instr. and Meth. A 563 (2006) 133.